NUCL SCI TECH (2020)31:78
https://doi.org/10.1007/s41365-020-00783-w

Attenuation characteristics of electromagnetic waves in plasma generated by coating radionuclide on surface structures

Sheng Lai[1] · Xiao-Bin Tang[1,2] · Jun-Xu Mu[1] · Zhao-Peng Feng[1] · Yun-Peng Liu[1,2]

Received: 19 April 2020 / Revised: 14 June 2020 / Accepted: 18 June 2020

Abstract Stealth technology plays an important role in modern military conflicts, especially when used in fighter jets. Since airfoil structures have a leading edge, inlet, and surface bulge that are easily detected by radar, it is necessary to study the stealth of these structures. In this study, we investigate structures coated with radionuclides to generate plasma. Using simulation and calculation methods, the attenuation of 0.1–10 GHz electromagnetic waves propagating in plasma was studied. The results showed that the attenuation of low-frequency electromagnetic waves is greater than that of high-frequency electromagnetic waves. The attenuation of 0.1–1 GHz electromagnetic waves is found to be less than − 2.7 dB, − 3.0 dB, and − 15.6 dB at the airfoil leading edge, inlet, and surface bulge structures, respectively. We also found that the attenuation of electromagnetic waves with 0°-incidence is greater than that of waves with 10°, 20°, and 30° incidence angles. Additionally, the attenuation of electromagnetic waves decreases gradually as the incident angle increases.

Keywords Plasma stealth · Radionuclide coating · Electromagnetic waves · Numerical simulation

✉ Xiao-Bin Tang
tangxiaobin@nuaa.edu.cn

[1] Department of Nuclear Science and Technology, Nanjing University of Aeronautics and Astronautics, Nanjing 210016, China

[2] Key Laboratory of Nuclear Technology Application and Radiation Protection in Astronautics, Ministry of Industry and Information Technology, Nanjing 210016, China

1 Introduction

At present, many countries have conducted extensive research on stealth technology, including RF stealth and optical stealth, which can be applied to advanced fighter jets [1–7]. Previous studies have shown that an airfoil leading edge, inlet, and surface bulge are easily detected by radar [8]. Therefore, it is necessary to investigate the stealth properties of these wing regions, including shape structure, radar jamming, and material stealth properties. Shape-structure stealth refers to the fighter jet surface, which is as parallel to the horizontal direction as possible for reducing the reflection of enemy radar electromagnetic waves. This results in an optimal smooth cone structure. Radar-jamming stealth refers to the proactive transmission of electromagnetic waves, by the fighter aircraft, with jamming characteristics determined after detecting and analyzing electromagnetic waves from enemy radar. This makes the enemy unable to obtain accurate information about fighter jet [9]. Material stealth refers to the coating of stealth materials on the surface of the fighter jet. These types of materials include ferrite, graphene, magnetic ultrafine metal powder, and polycrystalline iron fiber. The electromagnetic waves of enemy radar are absorbed and attenuated when transmitting to these stealth materials [10].

Because of the specificity of the above-mentioned structures, it is difficult to change them to achieve stealth. Compared with other stealth technologies, plasma stealth technology does not require the shape of a structure to be changed and has several advantageous properties, including wide absorption bandwidth, high absorptivity, and high adaptability [11]. Hence, plasma technology could be used to achieve stealth. The technology of plasma stealth was

Published online: 30 July 2020

first used in Russian Mig-144 fighter aircraft in the 1990s, and it demonstrated the viability of the technology. Song et al. [12] studied the electromagnetic wave propagation and scattering characteristics of the plasma sheath via high-order auxiliary differential equation-alternating direction implicit finite difference time domain (ADE-ADI FDTD) methods. The results of this study showed that the plasma sheath could reduce the backward radar cross section (RCS) at most frequency bands. Torrisi et al. [13] employed the finite element method (FEM) of electromagnetic waves to research propagation performance in strongly magnetized nonhomogeneous plasma. Their simulations showed that the propagation was strongly influenced by the plasma density profile. Zhang et al. [14] studied the attenuation characteristics of electromagnetic waves in multilayer plasma slabs, and they found that multilayer plasma slabs can effectively widen absorption bands, especially for low-frequency bands. Cheng et al. [15] researched the minimum energy to excite plasma coating for reducing the RCS of a target. Their results showed that the optimal electron density increased as the incident wave frequency increases.

The primary ways to produce plasma are arc discharge, laser irradiation, thermal ionization, and radionuclide excitation [16]. However, owing to energy limitations, arc discharge, laser irradiation, and thermal ionization cannot be employed to produce plasma in fighter aircraft. Since radionuclide decay does not consume energy, it is of great potential for plasma generation in fighter aircraft. Common radionuclide coatings with α-decay are Po-210 (5.3 MeV, 138.4d), Pu-238 (5.456 and 5.499 MeV, 87.7a), and Am-241 (5.443 and 5.485 MeV, 432.6a). The radionuclide coatings for β-decay are mainly Sr-90 (0.546 MeV, 28.5a) and Y-90 (2.288 MeV, 64 h) [17, 18]. The principle of radionuclide plasma production is that high-energy charged particles deposit their energy in gas, and gas ionization produces a large number of electron–ion pairs, forming plasma [19]. Flierl et al. [20] studied the energy deposition of alpha particles in hydrogen plasma. Their results showed that the electron density was positively correlated with the energy of the alpha particles. August [21] employed radioisotopes to produce plasma to reduce RCS. Vidmar [22] proposed a method of producing plasma by bombarding inertia gas with high-energy electron beams. It is necessary to study stealth by plasma generated by radionuclides coated on the airfoil leading edge, inlet, and surface bulge of fighter aircraft.

In this study, we research the stealth effect of these airfoil regions and simplify them to two-dimensional (2-D) models, as shown in Fig. 1, during calculation. The high-altitude fluid field is simulated by the computational fluid dynamics (CFD) method. Then, the energy deposition of radionuclide decayed particles is simulated by the Monte Carlo (MC) method. Finally, the attenuation of 0.1–10 GHz electromagnetic waves is calculated by the piecewise linear recursive convolution finite-difference time-domain (PLRC-FDTD) method. Through these methods, a complete research system of radionuclide-generating plasma for stealth in a high-altitude state is established.

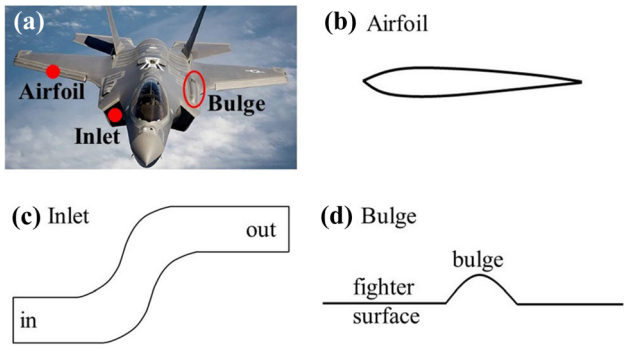

Fig. 1 (Color online) **a** Research object regions and 2-D simplified models of **b** airfoil, **c** inlet, and **d** bulge

Section 2 introduces the models and principles, including the calculation process and a detailed description of the various parameter settings. Section 3 presents and discusses the simulation results. Section 4 contains a summary of our study and the prospects for future work.

2 Simulation models and principle methods

The principle flowchart describing our simulation methodology is shown in Fig. 2. CFD simulations were used to provide atmosphere density distribution data for MC and numerical calculations.

In this work, we use alpha particles as an example, and the alpha particle energy deposition was obtained by MC simulation. By using the method of numerical calculation, we can calculate the maximum of electron–ion pairs from the energy deposition value. Because the mass of the ion is much larger than that of the electron, the oscillation effect of ions is not evident; therefore, we only need to consider electrons during our calculations. Because of recombination and diffusion, a portion of electrons will be lost. Therefore, it is necessary to establish a differential equation to calculate the equilibrium electron density, as shown in Fig. 2. The differential equation will be described in detail in Sect. 2.1. By adopting the Runge–Kutta fourth-order algorithm, we can solve this differential equation. The time gap of the Runge–Kutta fourth-order algorithm is the average time gap between the two adjacent ejected α-particles in one square centimeter. Plasma collision frequency was obtained by numerical calculation, and the plasma electron density and plasma collision frequency

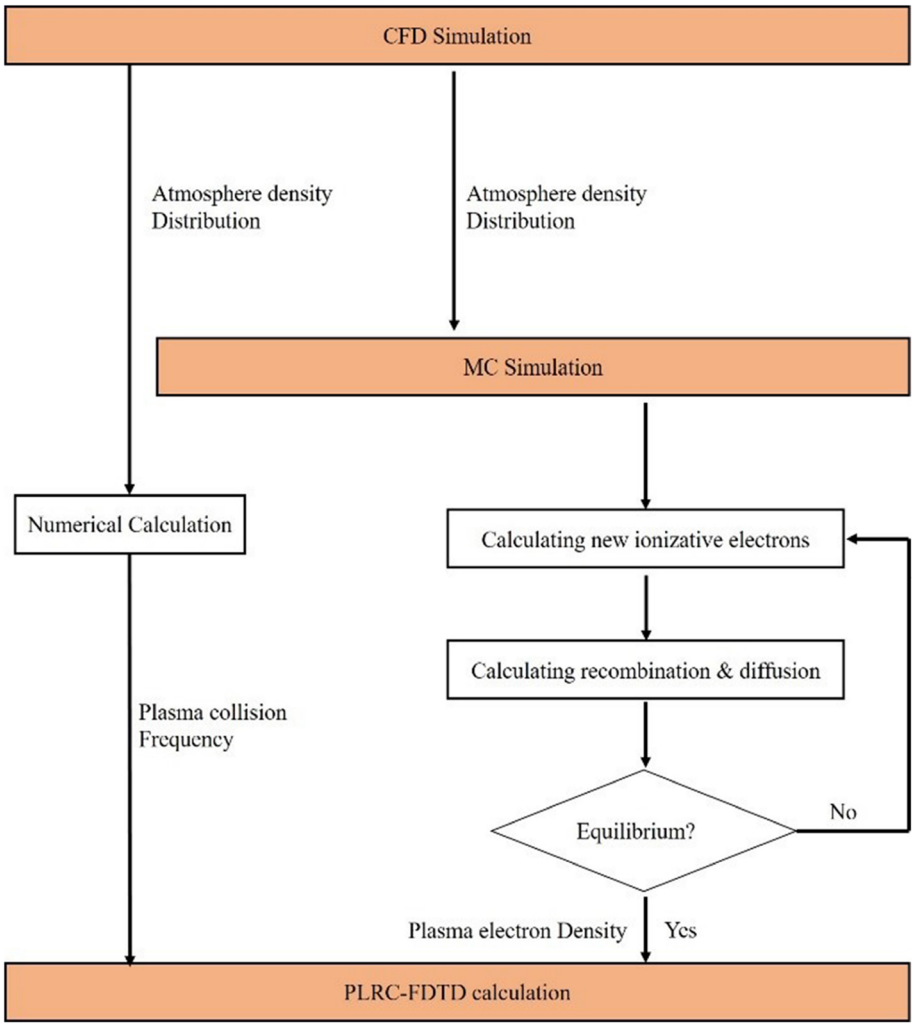

Fig. 2 Principle flow chart: the CFD simulation provides basic data for MC and PLRC-FDTD simulations

were used in the PLRC-FDTD algorithm to calculate the attenuation of electromagnetic waves by plasma.

2.1 Models of CFD and MC simulation

To obtain the air density distribution at the airfoil leading edge, inlet, and bulge, the structures were simplified to 2-D models during the calculation. In this work, we employed FLUENT, a computational fluid dynamics software, to simulate the air fluid field and used ANSYS ICEM CFD software to mesh these models, as shown in Fig. 3. To ensure that the models were as close as possible to the actual physical size of the structures, we set the model parameters to values as shown in Fig. 3. Because high-velocity fluid air is sensitive to the near-wall, the near-wall grid was densified, as shown in points A, B, and C in Fig. 3. In this study, we assumed that the fighter aircraft flies at an altitude of 20 km, where atmospheric pressure and temperature are 5529.3 Pa and 216.65 K, respectively [23], and the flight velocity is Mach 1.

To obtain alpha particle energy deposition, Geant4 was used to simulate the physical process of alpha particles in

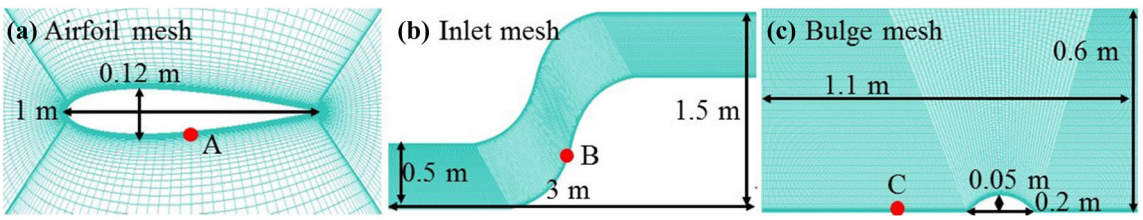

Fig. 3 (Color online) Model mesh of **a** airfoil, **b** inlet, and **c** bulge

atmosphere. Geant4 is an MC application package developed by CERN (European Organization for Nuclear Research) and based on C++ object-oriented technology [24, 25]. The MC simulation model was constructed, as shown in Fig. 4. Because the airfoil shape is flat, and we only study the energy deposition in front of the airfoil leading edge, we set the cuboid size to $0.1 \times 0.1 \times 0.6$ m^3, as shown in Fig. 4a, when calculating the energy deposition of the airfoil leading edge. We reset the MC calculation model as a cuboid ($0.5 \times 0.5 \times 0.6$ m^3) when calculating the energy deposition of the inlet and bulge. The cuboid is full of air, and the air density is obtained from a FLUENT simulation.

Considering that the emission direction of radioactive source particles is random, the MC simulation model is large, but we only pick up data in the red block ($0.1 \times 0.1 \times 0.6$ m^3) as shown in Fig. 4b as the calculation result of the inlet and bulge models. Horizontal incident electromagnetic waves can hit the bulge within only 5 cm of the fighter aircraft surface. Radionuclide-decay emission particles are isotropic, and we assume that the alpha particles are emitted from polonium-210, which releases 5.3 MeV alpha particles in this study. From the previous study [26], and because the air is thin at high altitude, we set the source activity as 100 Ci/cm^2. Previous studies [27, 28] have shown that the time of ionization producing electron–ion pairs is in the order of nanoseconds, and the time of recombination and diffusion is in the order of microseconds. Therefore, we consider the fighter aircraft to be stationary during the time of electron–ion pair production and recombination–diffusion.

2.2 PLRC-FDTD method of electromagnetic wave interaction with plasma

Researchers have studied the propagation characteristics of electromagnetic waves in plasma since the 1960s. These studies have proposed several finite difference time domain algorithms for electromagnetic simulation of dispersive media, including recursive convolution (RC), auxiliary equation (ADE), Z-transform, current density recursive convolution (JEC), Young's direct integration, and piecewise linear recursive convolution finite-difference time-domain (PLRC-FDTD). In the latter algorithm, the PLRC method has the advantages of strong adaptability, easy implementation, and high-calculation accuracy. In this study, the PLRC-FDTD method is adopted to calculate the attenuation characteristics of electromagnetic wave propagation in plasma. Before using the PLRC-FDTD method to calculate the interaction between electromagnetic waves and plasma [29, 30], we must first use

$$\omega_{\mathrm{p}} = \sqrt{\frac{n_{\mathrm{e}} \cdot e^2}{\varepsilon_0 \cdot m_0}}, \tag{1}$$

where ω_{p} is plasma electron oscillation frequency, e is electron charge, ε_0 is permittivity of free space, m_0 is electron static mass, n_{e} is equilibrium electron density, which can obtain by $N_{\max} = E_{\mathrm{d}} \cdot A / E_{\mathrm{i}}$ and $\mathrm{d}n_{\mathrm{e}}/\mathrm{d}t = N_{\max} - \alpha n_{\mathrm{e}}^2 - D_{\mathrm{dif}} \nabla n_{\mathrm{e}}$ [26] (where $N_{\max}$ is the maximum electron density, E_d is the particles energy deposition in the atmosphere, which obtained from MC simulation, A is radionuclide activity, and E_{i} is the average ionization energy, $E_{\mathrm{i}} = 35$ eV [19]; n_e is the equilibrium electron density, α is the recombination coefficient of positive and negative ions, $\alpha = 1.5 \times 10^{-6}$ cm^3/s [26], D_{dif} is the diffusion coefficient,$D_{\mathrm{dif}} = 370$ cm^2/s [26], and ∇n_{e} is the electron density gradient, obtained from CFD simulation), to calculate PLRC-FDTD parameters.

The collision frequency between electrons and neutral particles can be calculated by the following [31]:

$$\nu_{\mathrm{c}} = 5.2 \times 10^{12} \cdot P, \tag{2}$$

where ν_{c} is collision frequency, P is pressure [32] ($P = n_{\mathrm{e}} \cdot K \cdot T$), and n_{e}, K, and T are equilibrium electron density, Boltzmann constant, and temperature, respectively.

The Maxwell curl equation of electromagnetic wave in plasma can be written as [33]

$$\nabla \times H = \frac{\partial D}{\partial t} + \sigma E, \tag{3}$$

and

$$\nabla \times E = -\frac{\partial B}{\partial t} - \sigma_{\mathrm{m}} H, \tag{4}$$

where $B = \mu H, D(\omega) = \varepsilon(\omega) E(\omega)$, and μ and ε are the permeability and dielectric constants of plasma, respectively. The electric field value function with linear variation can be written as

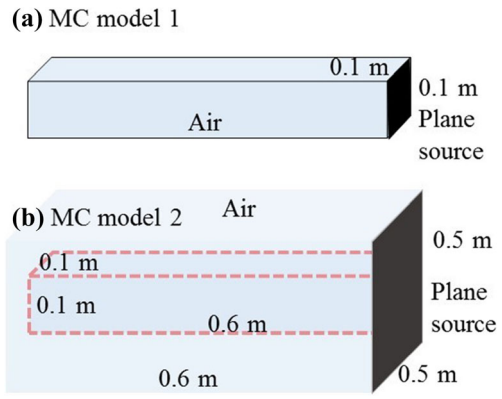

Fig. 4 MC simulation models used in **a** airfoil and **b** the inlet and bulge

$$E(t) = E^i + \frac{E^{i+1} - E^i}{\Delta t}(t - i\Delta t). \tag{5}$$

According to Fourier transform theory, D can be transformed to obtain the time domain form of the constitutive relation and then discretized in the time domain to obtain:

$$D(nt) = \varepsilon_0\varepsilon_\infty E(n\Delta t) + \varepsilon_0 \int_0^{n\Delta t} E(n\Delta t - \tau)\chi(\tau)\mathrm{d}\tau. \tag{6}$$

By substituting $n + 1$ for n in the form of a superscript, and subtracting it, we can obtain:

$$D^{n+1} - D^n = \varepsilon_0(\varepsilon_\infty + \chi_0 - \xi_0)E^{n+1} + \varepsilon_0(\xi_0 - \varepsilon_\infty)E^n - \varepsilon_0\psi^n. \tag{7}$$

The recursive form of ψ in Eq. (7) can be written as

$$\psi^{n+1} = C_\chi\psi^n + A_{\Delta\chi}E^{n+1} + B_{\Delta\chi}E^n. \tag{8}$$

Deriving the formula of electric field recurrence from Eqs. (3)–(8) yields:

$$E^{n+1} = \frac{\varepsilon_\infty - B_\chi}{\varepsilon_\infty + A_\chi}E^n + \frac{1}{\varepsilon_\infty + A_\chi}\psi^n + \frac{s\delta}{\varepsilon_\infty + A_\chi}\nabla \times H^{n+\frac{1}{2}}. \tag{9}$$

The upper physical quantities are

$$A_\chi = \chi_0 - \xi_0, \tag{10}$$

$$A_{\Delta\chi} = \Delta\chi_0 - \Delta\xi_0, \tag{11}$$

$$B_\chi = \xi_0, \tag{12}$$

$$B_{\Delta\chi} = \Delta\xi_0, \tag{13}$$

$$C_\chi = \exp(-\nu_c\Delta t), \tag{14}$$

$$\chi_0 = \frac{\omega_p^2}{\nu_c}\left[\Delta t - \frac{1}{\nu_c}(1 - \exp(-\nu_c\Delta t))\right], \tag{15}$$

$$\Delta\chi_0 = -\frac{\omega_p^2}{\nu_c^2}(1 - \exp(-\nu_c\Delta t))^2, \tag{16}$$

$$\xi_0 = \frac{\omega_p^2}{\nu_c}\left\{\frac{\Delta t}{2} - \frac{1}{\nu_c^2\Delta t}[1 - (1 + \nu_c\Delta t)\exp(-\nu_c\Delta t)]\right\}, \tag{17}$$

and

$$\Delta\xi_0 = -\frac{\omega_p^2}{\nu_c^3}(1 - \exp(-\nu_c\Delta t))[1 - (1 + \nu_c\Delta t)\exp(-\nu_c\Delta t)]. \tag{18}$$

From the above equations, we can see that they are related by ω_p and ν_c, which can be obtained from Eqs. (1) and (2). According to the requirements of numerical stability and dispersion [33], we set the time step, space step, and time stability factor as 0.125 ps, 75 μm, and 0.5, respectively. The plasma thickness is equal to the length of the MC model, and plasma grid numbers can be obtained from plasma thickness divided by the space step. There are five convolutional perfect matched layers on each side of the calculation space. A differential Gauss pulse source is used for electromagnetic wave signal, which has a pulse width τ = 30 Δt, where Δt is the time step, and the range of frequency is 0.1 to 10 GHz. The time domain electric field values are transformed into the frequency domain by Fourier transform. The meaning of E_{out} and E_{in} is shown in Fig. 5. The physical meaning of the transmission coefficient characterizes the extent to which the plasma attenuates electromagnetic waves. If the absolute value of the transmission coefficient is larger, the attenuation of electromagnetic waves is greater. The transmission coefficient is calculated by [34]

$$\mathrm{Att(dB)} = 20 \cdot \lg\frac{E_{out}}{E_{in}}. \tag{19}$$

3 Result and discussion

3.1 Validation of the PLRC-FDTD calculation method

To validate our PLRC-FDTD programming, it is necessary to compare our results with an example published in the literature [35]. In this example, the computational domain is divided into 800 cells, which includes 200 cells of plasma and 600 cells of free space. The space step is 75 μm and the time step is 0.125 ps, so the thickness of the computational domain is 6 cm, including 2 cm of plasma thickness. The plasma frequency is 1.8 × 10^{11} Hz, and the electron collision frequency is 2 × 10^{10} Hz. Electromagnetic waves with a range of 0.1–100 GHz are transmitted horizontally into the plasma region. The attenuation of electromagnetic waves can be calculated by Eq. (19). The schematic diagram of the validation model and the computational results are shown in Fig. 6. We set one boundary layer on each side of the computational domain with the plasma region in the middle of the domain.

Figure 6 shows a comparison of the attenuation calculated by PLRC-FDTD (indicated by the solid line) and the literature data (indicated by the red dotted line). Good

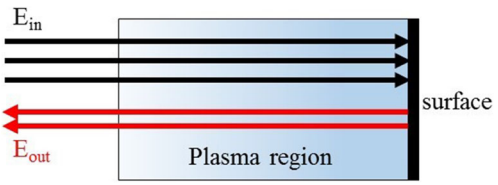

Fig. 5 (Color online) Schematic indicating the calculation process of the transmission coefficient

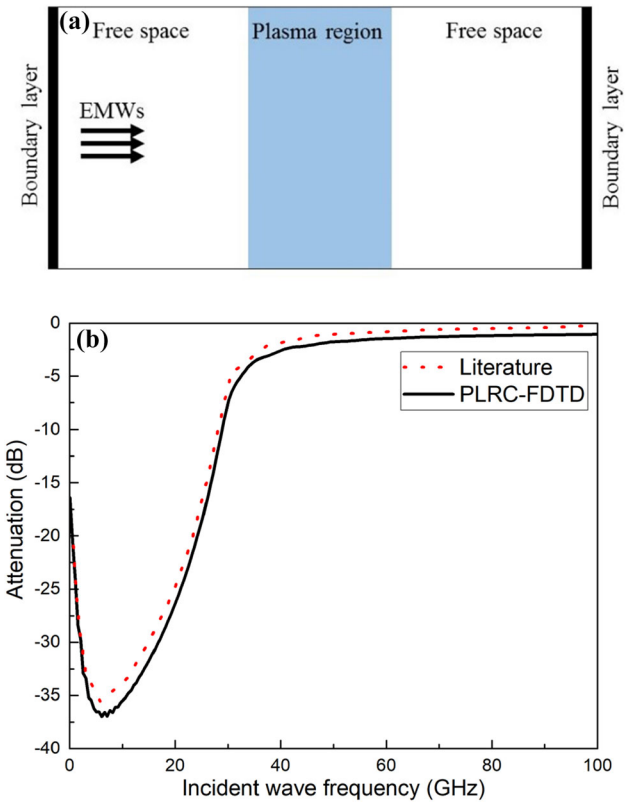

Fig. 6 **a** Schematic diagram of the validation model and **b** computational results

agreement is observed between our computational results and the literature results. This confirms that the programming method is correct in our study.

3.2 Attenuation performance of horizontal incident electromagnetic wave for the three structures

Using the models and the simulation software described in Sect. 2.1, we obtain the air density distribution of the airfoil leading edge, inlet, and surface bulge. Figure 7 shows the air density field distribution of these structures simulated by FLUENT software. The air density near the wall is high, such that the density of point B in Fig. 7a is higher than that of point A in the structure of the airfoil's leading edge. The situation is the same as shown in Fig. 7b, c. This is because when air flows in these structures, it will be blocked and squeezed near the wall, resulting in higher air density, as indicated by points B, D, and F. In this section, we assume that incident electromagnetic waves are horizontal, as shown in Fig. 7 (represented by the EMWs arrow). To obtain the air density value in the path of the electromagnetic waves, we set up three lines: AB, CD, and EF, with lengths of 0.6 m. The air density distribution is indicated by the dotted line in Fig. 8.

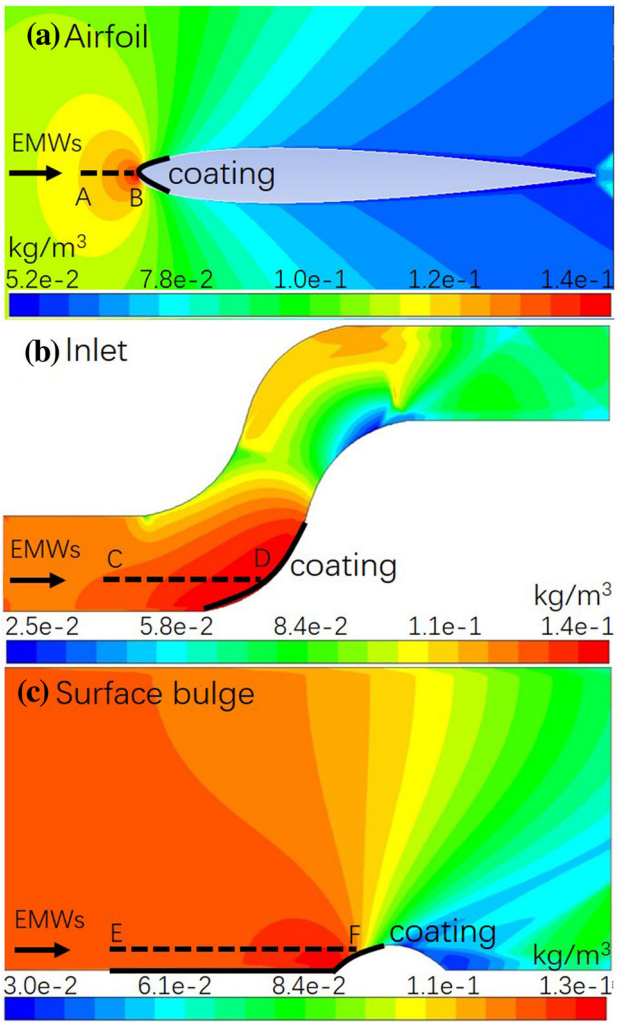

Fig. 7 (Color online) Air density field distribution of the **a** airfoil, **b** inlet, and **c** surface bulge

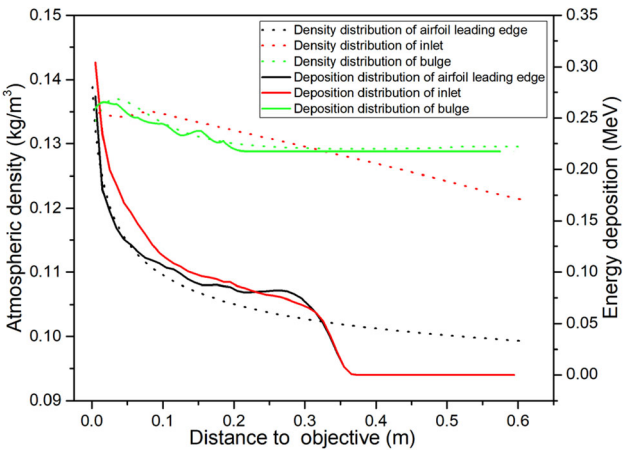

Fig. 8 (Color online) Air density distribution and MC simulation results

The dotted lines in Fig. 8 show that the maximum air density values of the three models are approximately equal

near the wall, with a value approximately equal to 0.135 kg/m^3. However, the air density distribution of the airfoil leading edge is different from the inlet and bulge. This is because the density values of the inlet and bulge are taken near the surface. Owing to the surface viscosity effect of the gas [28], air density near the wall is relatively high and the changing trend is relatively gentle.

According to the MC models and parameters described in Sect. 2.1, MC simulation results are shown in Fig. 8 and represented by a solid line. Figure 8 shows that where the air density is denser, the energy deposition of α particles is greater. Compared with the airfoil and inlet structures, we picked up the energy deposition value at a distance of 4 cm from the surface (line EF in Fig. 7), so the trend of energy deposition represented by the green solid line is relatively gentle in Fig. 8. The average range of 5.45 MeV α-particles is 3.84 cm in the air at normal pressure and temperature, and the track of a single α-particle is almost straight along the ejection direction [26]. However, because the air density is thin and pressure is far below normal pressure at high altitude, the average range of α-particles is approximately 35.1 cm.

Using the calculation method described in Sect. 2.2, we obtain the equilibrium electron density by using energy deposition values. Figure 9 shows the dependence of the equilibrium electron density on the distance to the objective. This value is similar to the energy deposition distribution in Fig. 8. The equilibrium electron density distribution is determined by the energy deposition distribution. Where the energy deposition is larger, the equilibrium electron density is smaller. The maximum equilibrium electron density is 3.43×10^{10} cm^{-3} and is located near the wall. With the increase in distance, the density of the equilibrium electron decreases rapidly. At the end of the range of α particle, the energy deposition is less such that the electron density is very thin. We believe that the matching of the plasma boundary and outer space is perfect. When calculating the equilibrium electron density of the bulge model, we need to calculate it in the normal direction of the bulge. This is because the electron diffusion is mainly in the normal direction.

Employing the PLRC-FDTD calculation method and parameter settings described in Sect. 2.2, we calculate the attenuation of incident electromagnetic waves, the results of which are shown in Fig. 10. The attenuation of the incident electromagnetic waves is determined by the plasma frequency, plasma collision frequency, and thickness of plasma. Figure 10 shows that the electromagnetic wave attenuation of the airfoil and inlet are less than the attenuation of the bulge. This is because the density and thickness of the plasma are relatively small in the airfoil and inlet models. The attenuation of electromagnetic waves is approximately 3 dB at a range of 0.1–1 GHz for the airfoil and inlet. The attenuation of electromagnetic waves decreases with the increase in wave frequency. This is because when the frequency of the electromagnetic wave is greater than the plasma frequency and the collision frequency calculated by Eqs. (1) and (2) the interaction between electromagnetic waves and plasma is relatively weak such that the attenuation is low.

When the plasma frequency calculated by Eq. (1) is greater than the frequency of the electromagnetic waves, the attenuation is greater. Moreover, the frequency of electromagnetic waves is close to the plasma collision frequency calculated by Eq. (2), which leads to the generation of the resonance effect, and the plasma is considered to be a stopband [36, 37]. Therefore, for the bulge model, it has a maximum attenuation at 0.5 GHz and a value of − 23 dB. The plasma collision frequency is 0.53 GHz, and the attenuation of electromagnetic waves is less than − 15 dB at a range of 0.1–1 GHz. The attenuation of electromagnetic waves decreases gradually with the

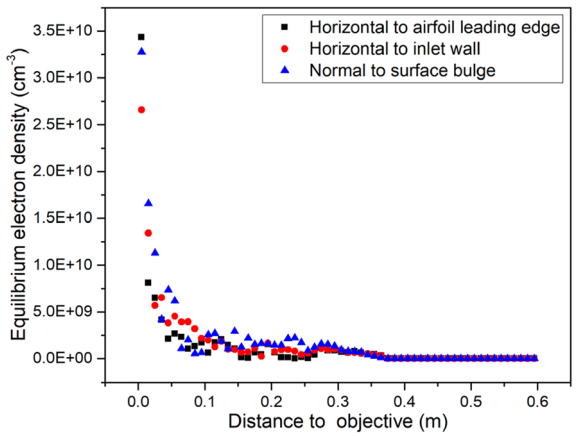

Fig. 9 (Color online) Dependence of the equilibrium electron density on the distance to the objective

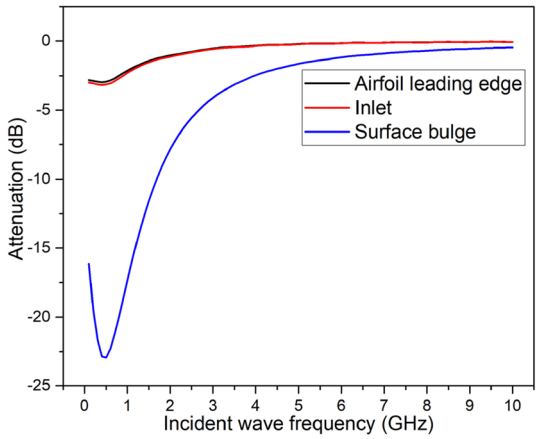

Fig. 10 (Color online) Dependence of the attenuation of electromagnetic waves on the incident wave frequency

increase in electromagnetic wave frequency. Figure 10 indicates that the stealth effect of the bulge structure is better than that of the airfoil and inlet structures under the same frequency of incident electromagnetic waves.

3.3 Attenuation performance of different incident angles of electromagnetic waves on the bulge structure

In this section, we assume that electromagnetic waves propagate toward the bulge at different angles. The schematic diagram indicating the incident direction of the electromagnetic waves is shown in Fig. 11 (represented by the EMWs arrow). To compare results with those in Sect. 3.2, we also set the length of the plasma region to 0.6 m. The calculation methods of electron density and collision frequency are the same as described in Sect. 3.2. The attenuation of electromagnetic waves with different angles is calculated, and the results are shown in Fig. 12.

Figure 12 shows the dependence of the attenuation of electromagnetic waves on the wave frequency for different incident angles. The attenuation of electromagnetic waves decreases with the increase in the incident angle. This is because the equilibrium electron density away from the surface is relatively thin compared with the equilibrium electron density near the surface, as shown in Fig. 9. Compared with the line-0°, the electromagnetic wave attenuation trends of line-10°, line-20°, and line-30° are similar. Because the plasma characteristics at line-10°, line-20°, and line-30° are approximately equal, when electromagnetic waves propagate at these regions, the electromagnetic wave attenuation by the plasma is also approximately equal. However, the closer the plasma is to the surface, the higher the plasma electron density. For line-0°, line-10°, line-20°, and line-30°, the attenuation relationship of electromagnetic waves is line-0° > line-10° > line-20° > line-30°. Because the electron density of line-0° is more uniform and denser, the attenuation of electromagnetic waves at the line-0° region is relatively large.

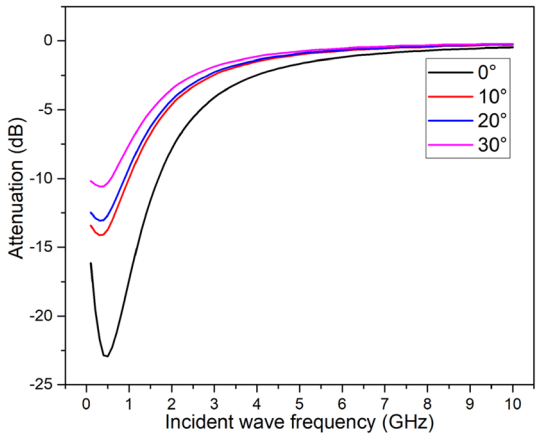

Fig. 12 (Color online) Dependence of the attenuation of electromagnetic waves on the wave frequency for different incident angles

These results show that when a fighter aircraft is flipping, climbing, or diving, it is more easily detected by enemy radar. For the 0.1–1 GHz electromagnetic wave, its attenuation is lower than − 15, − 13, − 12.5, and − 10 dB, with incidence angles of 0°, 10°, 20°, and 30°, respectively. However, for 7–10 GHz electromagnetic waves, the attenuation of electromagnetic waves is approximately − 1 dB for the four angles. This is because, when the frequency of the incident electromagnetic wave is much greater than the collision frequency of the plasma, the resonance attenuation effect between the electromagnetic wave and the plasma electron is very weak such that the electromagnetic wave can almost pass through the plasma without attenuation. This shows that for higher frequency electromagnetic waves, the stealth effect of plasma is not significant. Table 1 shows the maximum

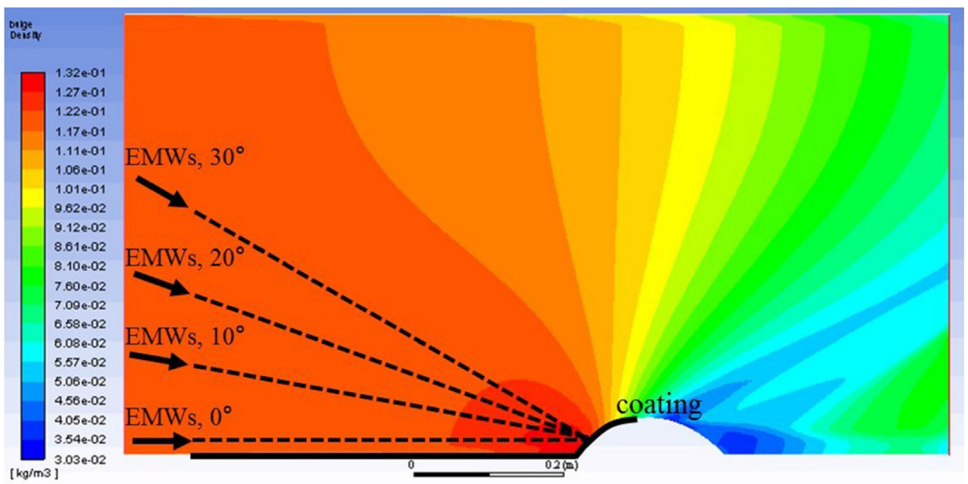

Fig. 11 (Color online) Schematic diagram indicating the incident direction of electromagnetic waves

Table 1 Maximum attenuation of electromagnetic waves and corresponding wave frequencies under different incident angles

Parameters	Incident angles (°)			
	0	10	20	30
Maximum attenuation (dB)	− 23	− 14.1	− 13.1	− 10.4
Frequency (GHz)	0.5	0.32	0.28	0.2

attenuation of electromagnetic waves and the corresponding wave frequencies under different incident angles. The electromagnetic wave frequency corresponding to the maximum attenuation value moves to the low-frequency band with the increase in incident angle. Figure 12 indicates that when coating fighter aircraft structures with radionuclides, electromagnetic waves in the low-frequency band can be seriously attenuated by plasma.

4 Conclusion

In this study, we investigate the attenuation of electromagnetic waves propagating in plasma on different structures and at different incidence angles. CFD, MC, and PLRC-FDTD methods were used to determine the performance of electromagnetic wave attenuation at these structures and incidence angles. By simplifying the structures to 2-D models during the calculation, we obtained the air density distribution by CFD simulation. The energy deposition of α-particles in the air was calculated by the MC method, and the plasma frequency and collision frequency were obtained by the numerical calculation method. The PLRC-FDTD algorithm was employed to calculate the attenuation of electromagnetic wave propagation in plasma. Our results show that the air density decreases with the increase in the distance in the normal direction of these structures, and the high-density air concentrates mainly near the wall. Because the energy deposition of alpha particles is nearer to the wall, dense plasma is produced there. Compared with the attenuation at the airfoil leading edge and inlet, the attenuation of electromagnetic waves at the surface bulge is larger, and the attenuation of low-frequency electromagnetic waves is significant. However, when the frequency of electromagnetic wave increases, the attenuation of electromagnetic waves gradually decreases. Moreover, the attenuation of the electromagnetic wave decreases with the increase in the incident angle at the bulge structure, which indicates that the stealth effect is present for horizontally incident electromagnetic waves.

In this work, we established a complete simulation research system for radionuclide producing plasma in a high-altitude state. Although the attenuation of electromagnetic waves at different structures and angles can be determined by the methods used in this study, further research needs to be conducted to consider other factors, such as flight altitude, the activity and type of radioactive source, and the shape of the radioactive source [38, 39]. Plasma coatings with infrared stealth materials have great potential for reducing infrared radiation. In addition, it is very important to study the application of plasma to radomes in the future.

References

1. X. Wang, J.Z. Zhu, W. Liu, Radar scattering width effects by coating ^{90}Sr/^{90}Y layers on cylindrical targets. Nucl. Sci. Tech. **28**, 22–29 (2017). https://doi.org/10.1007/s41365-017-0196-9
2. R.J. Vidmar, On the use of atmospheric pressure plasmas as electromagnetic reflectors and absorbers. IEEE Trans. Plasma Sci. **18**, 733–741 (1990). https://doi.org/10.1109/27.57528
3. H.F. Zhang, S.B. Liu, The properties of unusual surface plasmon modes and switching gaps in the three-dimensional photonic crystals composed of plasma-coated spheres. J. Electromagn. Waves Appl. **28**, 1347–1359 (2014). https://doi.org/10.1080/09205071.2014.921124
4. H. Li, X.B. Tang, S. Hang, Potential application of X-ray communication through a plasma sheath encountered during spacecraft reentry into earth's atmosphere. J. Appl. Phys. **121**, 123101 (2017). https://doi.org/10.1063/1.4978758
5. S. Hang, Y.P. Liu, H. Li, Temporal characteristic analysis of laser-modulated pulsed X-ray source for space X-ray communication. Nucl. Instrum. Methods Phys. Res. Sect. A Accel. Spectrometers Detect. Assoc. Equip. **887**, 18–26 (2018). https://doi.org/10.1016/j.nima.2018.01.031
6. G. Xia, L. Yang, The study on infrared stealthy of variable emissivity materials based on the radiation contrast. Appl. Mech. Mater. **419**, 341–347 (2013). https://doi.org/10.4028/www.scientific.net/AMM.419.341
7. X.J. Zhang, S.L. Wang, H.M. Jia et al., A high sensitivity screening method for γ peaks based on the critical level. Nucl. Tech. **42**, 070202 (2019). https://doi.org/10.11889/j.0253-3219.2019.hjs.42.070202. (**in Chinese**)
8. K.Z. Yue, S.C. Chen, W.L. Liu, Simulation of conceptual designs of a three-surface stealth strike fighter. Int. J. Aeronaut. Space Sci. **15**, 366–373 (2014). https://doi.org/10.5139/ijass.2014.15.4.366
9. B. Bai, Y. Liu, L. Song, Passive radar jamming: a novel method using time-varying plasma. IEEE Access. **7**, 120082–120088 (2019). https://doi.org/10.1109/ACCESS.2019.2935514
10. M. Rahmanzadeh, H. Rajabalipanah, A. Abdolali, Analytical investigation of ultrabroadband plasma-graphene radar absorbing structures. IEEE Trans. Plasma Sci. **45**, 945–954 (2017). https://doi.org/10.1109/TPS.2017.2700724
11. K. Ozkan, S.G. Cigdem, Response of magnetized plasma having linearly varying electron density profile to oblique electromagnetic wave incidence. J. Electromagn. Waves Appl. **32**, 2046–2054 (2018). https://doi.org/10.1080/09205071.2018.1489311
12. W.J. Song, H. Zhang, Analysis of electromagnetic wave propagation and scattering characteristics of plasma shealth via high order ADE-ADI FDTD. J. Electromagn. Waves Appl. **30**,

1321–1333 (2016). https://doi.org/10.1080/09205071.2016.1198727
13. G. Torrisi, D. Mascali, G. Sorbells, Full-wave FEM simulations of electromagnetic waves in strongly magnetized non-homogeneous plasma. J. Electromagn. Waves Appl. **28**, 1085–1099 (2014). https://doi.org/10.1080/09205071.2014.905245
14. Q.C. Zhang, Z.Y. Tian, Study of attenuation characteristics of electromagnetic waves in multilayer plasma slabs. J. Appl. Phys. **125**, 094902 (2019). https://doi.org/10.1063/1.5037417
15. D. Cheng, H.C. Yin, H.X. Zheng, Research on minimum energy excited to plasma coating for reducing radar cross section of target. Prog. Electromagn. Res. Lett. **83**, 15–22 (2019). https://doi.org/10.2528/pierl16012503
16. H. Li, X.B. Tang, S. Hang, High-directional laser-plasma-induced X-ray source assisted by collimated electron beams in targets with a self-generated magnetic field. Fusion Eng. Des. **144**, 193–201 (2019). https://doi.org/10.1016/j.fusengdes.2019.05.001
17. C. Zhu, J. Zhang, A.M. Chen, The adsorption transfer mechanism of U and 238Pu in sandy aquifers. Nucl. Tech. **42**, 090301 (2019). https://doi.org/10.11889/j.0253-3219.2019.hjs.42.090301. **(in Chinese)**
18. X.Y. Deng, Y.D. Su, X.G. Tuo, Adsorption characteristics of 239Pu in Dachaidan clay rocks in Qinghai. Nucl. Tech. **42**, 080304 (2019). https://doi.org/10.11889/j.0253-3219.2019.hjs.42.080304. **(in Chinese)**
19. P.J. William, The ionization by polonium alpha particles in air and the average energy to make an ion pair. Radiat. Res. **13**, 1–17 (1960). https://doi.org/10.2307/3570868
20. H.P. Flierl, M. Engelbrecht, The energy loss of alpha particles traversing a hydrogen plasma. Nucl. Instrum. Methods Phys. Res. Sect. A Accel. Spectrometers. Detect. Assoc. Equip. **415**, 637–641 (1998). https://doi.org/10.1016/s0168-9002(98)00438-0
21. H. August, U.S. Patent 3,713,157, 23 Jan 1973
22. Vidmar, U.S. Patent 5,594,446, 14 Jan 1997
23. National oceanic and atmospheric administration, *U.S. standard atmosphere*. (U.S. Government Printing Office, 1976)
24. A. Munoz, J.M. Perez, An approach to Monte Carlo simulation of low-energy electron and photon interactions in air. Nucl. Instrum. Methods Phys. Res. Sect. A Accel. Spectrom. Detect. Assoc. Equip. **536**, 176–188 (2005). https://doi.org/10.1016/j.nima.2004.07.171
25. A. Hussain, S.M. Mirza, Beta-efficiency of a typical gas-flow ionization chamber using Geant4 monte carlo simulation. Nucl. Technol. Radiat. Prot. **26**, 193–200 (2011). https://doi.org/10.2298/NTRP1103193H
26. W. Liu, J.Z. Zhu, Influence of plasma induced by radionuclide layer on the radar cross section of spherical objects. Nucl. Sci. Tech. **26**, 040502 (2015). https://doi.org/10.13538/j.1001-8042/nst.26.040502
27. A. Bourdon, Y. Teresiak, P. Vervisch, Ionization and recombination rates of atomic oxygen in high-temperature air plasma flows. Phys. Rev. E **57**, 4684–4692 (1998). https://doi.org/10.1103/PhysRevE.57.4684
28. S.A. Losev, V.A. Polyanskii, Nonequilibrium ionization of air behind a shock wave front at speeds of 5–10 km/s. Fluid Dyn. **3**, 176–183 (1968). https://doi.org/10.1007/bf01016258
29. J.L. Young, R.O. Nelson, A summary and systematic analysis of FDTD algorithms for linearly dispersive media. IEEE Antennas Propag. Mag. **43**, 61–77 (2001). https://doi.org/10.1109/74.920019
30. R.J. Luebbers, F. Hunsberger, A frequency-dependent finite-difference time-domain formulation for transient propagation in plasma. IEEE Trans. Antennas Propag. **39**, 29–34 (1991). https://doi.org/10.1109/8.64431
31. S.B. Liu, J.J. Mo, N.C. Yuan, FDTD analysis of reflection of electromagnetic wave from a conductive plane covered with inhomogeneous time-varying plasma. Plasma Sci. Technol. **5**, l669–1676 (2003). https://doi.org/10.1088/1009-0630/5/1/011
32. Z. Wang, L Guo, W Chen, The influence of non-uniform flow field characteristics of hypersonic vehicle on electromagnetic wave propagation. Paper presented at 2018 International Applied Computational Electromagnetics Society Symposium (ACES), Beijing, China, 29 July–1 August 2018
33. D.F. Kelley, R.J. Luebbers, Piecewise linear recursive convolution for dispersive media using FDTD. IEEE Tram Antennas Propgat. **44**, 792–797 (1996). https://doi.org/10.1109/8.509882
34. C.H. Lan, X.W. Hu, Z.H. Jiang, Interaction of electromagnetic waves with two-dimensional metal covered with radar absorbing material and plasma. Plasma Sci. Technol. **10**, 717–723 (2008). https://doi.org/10.1088/1009-0630/10/6/12
35. J.S. Jia, C.X. Yuan, S. Liu, Propagation of electromagnetic waves in a weak collisional and fully ionized dusty plasma. Phys. Plasmas **23**, 043302 (2016). https://doi.org/10.1063/1.4946780
36. Y. Xu, X. Qi, PIC-MCC simulation of electromagnetic wave attenuation in partially ionized plasmas. Plasma Sour. Sci. Technol. **23**, 015002 (2014). https://doi.org/10.1088/0963-0252/23/1/015002
37. C.X. Yuan, Z.X. Zhou, Reflection properties of electromagnetic wave in a bounded plasma slab. IEEE Trans. Plasma Sci. **38**, 3348–3355 (2010). https://doi.org/10.1109/tps.2010.2084110
38. N. Luo, J.S. Zhang, B.H. Liang et al., Radionuclides separation and analysis after ThO_2 irradiation in reactor. Nucl. Tech. **42**, 080605 (2019). https://doi.org/10.11889/j.0253-3219.2019.hjs.42.080605. **(in Chinese)**
39. L.W. Han, K. Li, G.Q. Zhong et al., Metal material activation research on EAST fusion facility. Nucl. Tech. **42**, 050604 (2019). https://doi.org/10.11889/j.0253-3219.2019.hjs.42.050604. **(in Chinese)**